Sea Ice Melting and Floe Geometry in a Simple Ice-Ocean Model

Michael Steele

Polar Science Center, Applied Physics Laboratory, College of Ocean and Fishery Sciences, University of Washington, Seattle

A coupled sea ice-ocean numerical model has been developed that addresses the role of floe geometry during summertime melting. The model contains a diagnostic equation for average floe diameter in addition to the usual prognostic equations for ice volume per unit area and ice concentration. The partition between melting on the top, bottom, and lateral (side) surfaces of floes is examined using time-dependent simulations with differing initial average floe diameters. The different parameterizations for bottom and lateral melting in the literature are also compared and found to vary significantly. The results show that lateral melting is important only for floes with diameters less than $O(30\ m)$, given atmospheric thermal forcing typical of the central Arctic in summer. This means that the decrease in ice concentration over the summer is a strong function of floe diameter, in keeping with simple geometrical arguments. In all cases, about 80% of the net thermal energy that enters the ocean through leads goes toward melting ice, while the rest warms the ocean.

1. Introduction

The summer sea ice cover is a jumbled ensemble of floes of various sizes and shapes floating on the ocean surface. Figure 1 shows an example, a digitized photomosaic obtained during the Arctic Ice Dynamics Joint Experiment (AIDJEX) in the Beaufort Sea [*Rothrock and Thorndike*, 1984]. The volume of ice in a particular region is usually given by the distribution function $g(H)$, which describes the fractional cover of ice of thickness H [*Thorndike et al.*, 1975]. More commonly, numerical models use two state parameters for the amount of ice in a given region: h, the "equivalent thickness" (volume of ice divided by the surface area of the region), and A, the areal concentration of ice of thickness greater than some threshold h_0 (usually taken as 0.5 m) [*Hibler*, 1979, hereinafter "H79"]. These parameters are adequate to describe exchange processes in the air-ice-ocean system if one considers only the top and bottom surfaces of the floes. However, transfer also occurs at the edges of floes. *Steele et al.* [1989a], for example, discuss how lateral stresses affect floe velocity. Similarly, floe melt rates are affected by heat transfer on the top, bottom, and lateral faces. This paper describes a numerical model that considers this heat partition for a simple case.

Consider the idealized states depicted in Figures 2a and 2b, in which the sea ice cover consists of uniform floes of a given diameter. The areal coverage is approximately the same in both cases. Assume that the floe thicknesses are also identical. Now ask, "For the same (atmospheric) thermal forcing, how will the melt rates differ for Figures 2a and 2b?" Intuitively, we expect more melting for Figure 2a because the total perimeter, or lateral surface area, is greater than in Figure 2b although the top and bottom surface areas are the same. Thus the areal coverage should decrease faster for Figure 2a.

The numerical models of sea ice presently in use are unable to distinguish between the states shown in Figures 2a and 2b [e.g., H79; *Mellor and Kantha*, 1989, hereinafter "MK89"]. These models do not contain an explicit treatment of floe geometry such as an equation for the floe diameter. Half the heat that enters the ocean through leads is assumed to cause a decrease in ice concentration, while the other half decreases ice thickness. This relationship is fixed for all time in these models.

In the model described here, the melt rates on the top, bottom, and lateral floe surfaces are calculated independently. The heat

balances on each ice surface are computed using the observations and models of *Maykut and Perovich* [1987] (hereinafter "MP87") on the heat budget of summer leads. The role of the molecular sublayer at the ice-ocean interface [*McPhee et al.*, 1987] is also included. For leads less than several hundred meters wide, MP87 found that the total melt rate, as well as the partition between top, bottom, and lateral melting, depended on the initial width of the lead. Their results were expressed in terms of the growth rate of a single lead's width during a period of solar heating. With a view toward larger-scale modeling, the results here are expressed in terms of an ensemble of floes that experience changes in thickness and diameter. In this context we ask the question, "How important is lateral melting in the overall melt rate of the sea ice cover?"

The equations for the ice and ocean models are discussed in section 2, along with the heat, salt, and momentum coupling between the models. The numerical simulations and their results are presented in section 3. Section 4 contains a discussion of the results.

2. Theory

2.1. Sea Ice Model

To estimate the partition of fluxes between top, bottom, and lateral ice floe surfaces, we need to know the relative amount of each type of surface area. The first step is to find a horizontal length scale for a floe that can be related to these surface areas. Following *Rothrock and Thorndike* [1984], we define the "mean caliper diameter" L as the average over all angles of the distance between two parallel lines (or calipers) that are set against the floe's sidewalls. For a circle, L is the diameter as usually defined; for a square, L is intermediate between the length of a side and the diagonal.

The top surface area of each floe will be referred to as the "horizontal surface area" (equal to the bottom surface area), in contrast to the "lateral surface area" around the sides of the floe. The concept of mean caliper diameter allows us to use the general result that

$$p = \pi L \qquad (1)$$

for any convex shape, where p is the perimeter. Rothrock and Thorndike found that for Figure 1 the ratio p/L had a mean of 3.17 and standard deviation of only 0.04; i.e., floes were largely convex. Note, however, that the smallest floes they digitized from the photomosaic were approximately 1 km in diameter. It is assumed in this paper that the geometrical properties found by

Rothrock and Thorndike for Figure 1 extend to smaller scales. This seems reasonable considering their discussion of the scale invariance of floe geometry (see their Figure 4), but also suggests the need for further observations.

Unfortunately, there is no simple relation like (1) for s, the horizontal surface area. Rothrock and Thorndike found that

$$s = \alpha L^2 \qquad (2)$$

where the mean value of $\alpha = 0.66$ (and standard deviation $= 0.05$). This is the value used here; sensitivity experiments are discussed in section 3.

If we assume that melting occurs uniformly at a rate w_{lat} around the perimeter of the flow,

$$\frac{ds}{dt} = w_{lat} p \qquad (3)$$

Substituting from (1) and (2) then gives

$$\frac{dL}{dt} = \frac{\pi}{2\alpha} w_{lat} \qquad (4)$$

which relates the loss of average floe diameter dL/dt to the sidewall melt rate w_{lat}.

We now turn our attention from the geometry of single floes to parameters that describe an ensemble of such floes in a given region. The areal concentration a is the ratio of ice-covered horizontal area containing n floes of a particular diameter to the total horizontal surface area s_{tot} in a region; i.e.,

$$a = \frac{n s}{s_{tot}} \qquad (5)$$

The total concentration A is the sum of a over all diameters. For a region containing floes with only a single diameter L,

$$A = \frac{n}{s_{tot}} s(L) \qquad (6a)$$

$$A = \frac{n}{s_{tot}} \alpha L^2 \qquad (6b)$$

$$A = \frac{A_0 L^2}{L_0^2} \qquad (6c)$$

where the subscript "0" in (6c) refers to the initial condition and n is assumed to be constant. The analogous quantity for the ratio of lateral surface area to total horizontal surface area is $A_L = A \pi H / \alpha L$, where H is the ice thickness.

In this paper, the sea ice cover is assumed to be well described by a single "average diameter." Figure 3 illustrates several possible distributions of n/s_{tot} with respect to floe diameter. In Figure 3a a delta function at L represents a field of floes with identical diameters, such as observed in parts of the marginal ice zone (MIZ) [Wadhams et al., 1988]. Figure 3b illustrates a uniform distribution of diameters from 0 m to twice the average value L. This is analogous to the distribution assumed by H79 for ice thickness during melting. In this case, concentration a varies as the square of diameter. Figure 3c shows the distribution that corresponds to Figure 1; for this plot, the floes in Figure 1 were digitized down to about 30 m diameter (D. A. Rothrock, personal communication, 1992). This distribution is a strong function of diameter; i.e., there are many more small floes than large ones; in this case, ice concentration a is a weakly decreasing function of
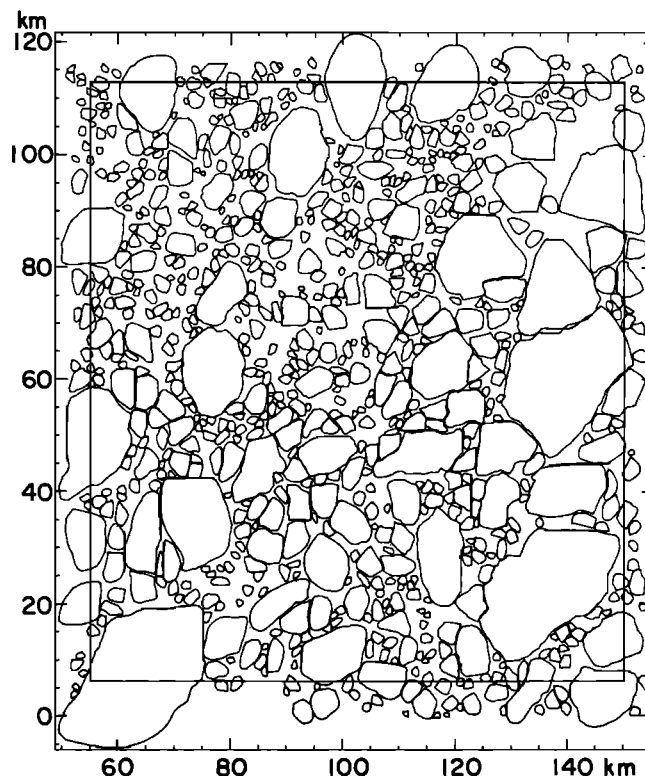

Fig. 1. Digitized floe boundaries from a mosaic of aerial photographs of summer pack ice in the Beaufort Sea [Rothrock and Thorndike, 1984].
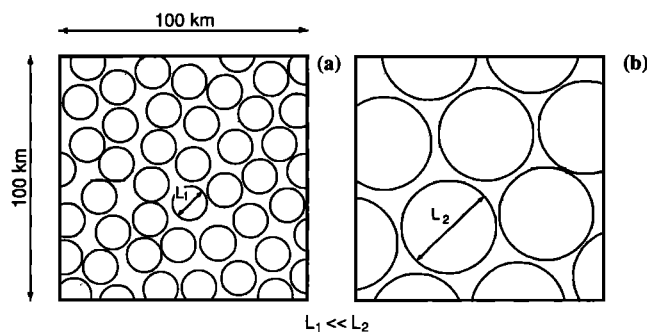

Fig. 2. An idealized pair of sea ice states (plan view). Solar heating of the ice-ocean system leads to a different response for each state, depending on the total ice floe perimeter. Standard numerical models cannot differentiate between states (a) and (b).

diameter. The concept of "average diameter" is most obviously applicable to Figures 3a and 3b. An average diameter may, of course, also be defined for Figure 3c, but it is not sufficient to describe the distribution completely [Rothrock and Thorndike, 1984]. The applicability of the present model to this case is discussed further in section 3.

We consider here the changes in the sea ice state due to melting only. When other processes such as advection, internal ice stress, and freezing are neglected, the prognostic equations for sea ice volume AH and total concentration A in a given region become

$$\frac{d}{dt}(AH) = A \left[w_{top} + w_{bot} + \frac{\pi H}{\alpha L} w_{lat} \right] \qquad (7)$$

and

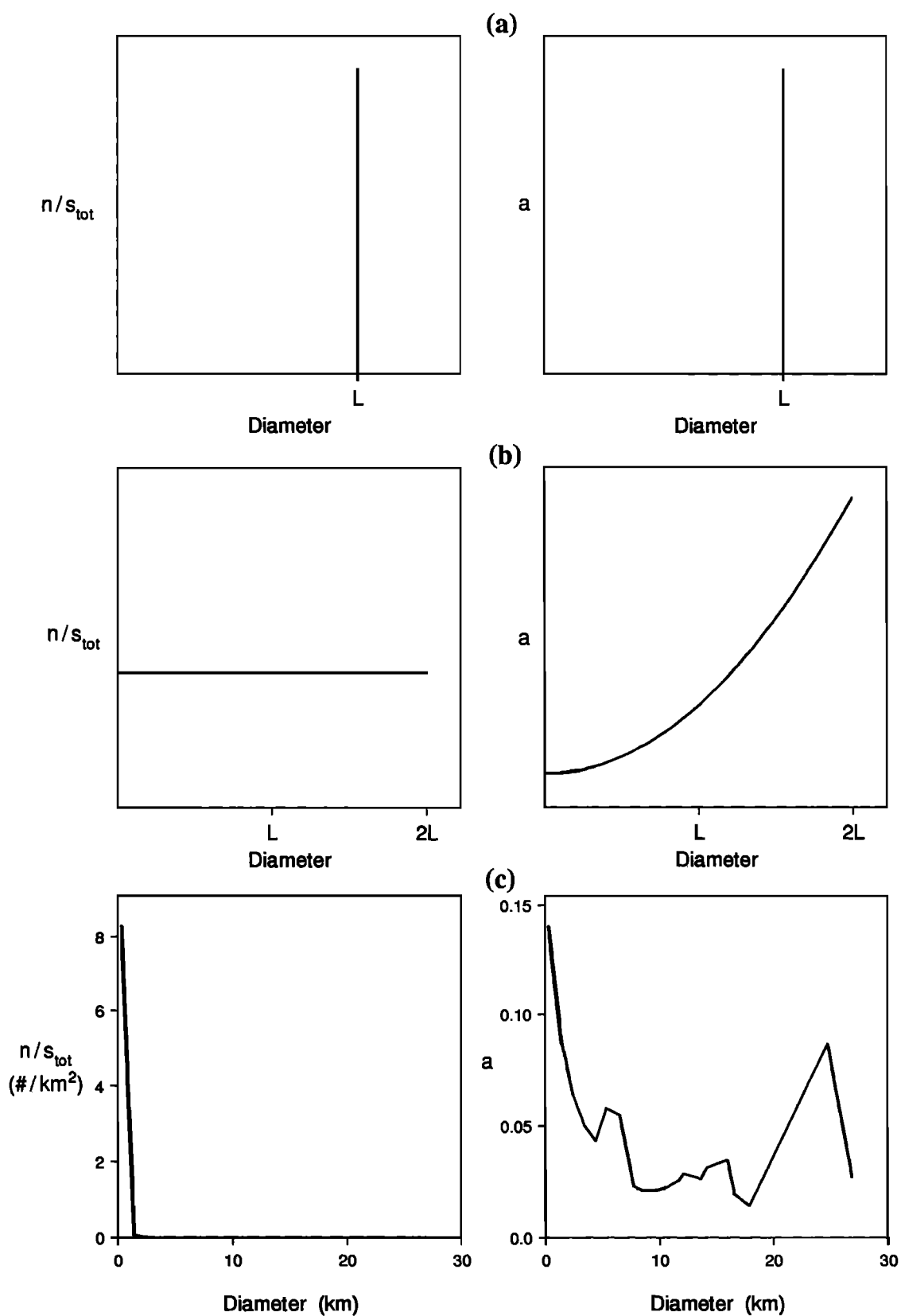$$H \frac{dA}{dt} = A \frac{\pi H}{\alpha L} w_{lat} \qquad (8)$$

Fig. 3. Three possible distributions of floe diameters L, in terms of (left) the number per unit area n/s_{tot} and (right) the (horizontal) areal concentration a. (a) Only one diameter as observed in the marginal ice zone. (b) Uniform distribution between 0 and $2L$, where L is the average diameter. (c) Distribution and concentration corresponding to Figure 1 for a region of the Beaufort Sea on August 18, 1975.

where w is the melt rate on each ice surface. Figure 4 illustrates the heat and salt fluxes (described below) associated with each melt rate. Note that in (7) the role of lateral melting is negligible for $\pi H / \alpha L << 1$; i.e., large floes melt mostly from top and bottom surfaces and produce little change in areal concentration. Equation (8) follows from differentiation of (6a) with respect to time and substitution from (1), (3), and (6b). The main difference between prognostic equations (7) and (8) and those used in models such as H79's and MK89's without an explicit treatment of floe geometry is in the lateral melting terms. Instead of the w_{lat} term, those models use an expression that is proportional to the total heat flux at the ocean surface. MK89 partition this flux equally between sink terms for ice thickness and ice concentration via their parameter Φ_m, to which their results were fairly sensitive. H79 assumes a uniform distribution of ice thicknesses during melting, which leads to sink terms similar (although not identical) to those of MK89. This assumption can be compared with the rather complex seasonal thickness distributions observed in the Arctic by *Bourke and Garrett* [1987].
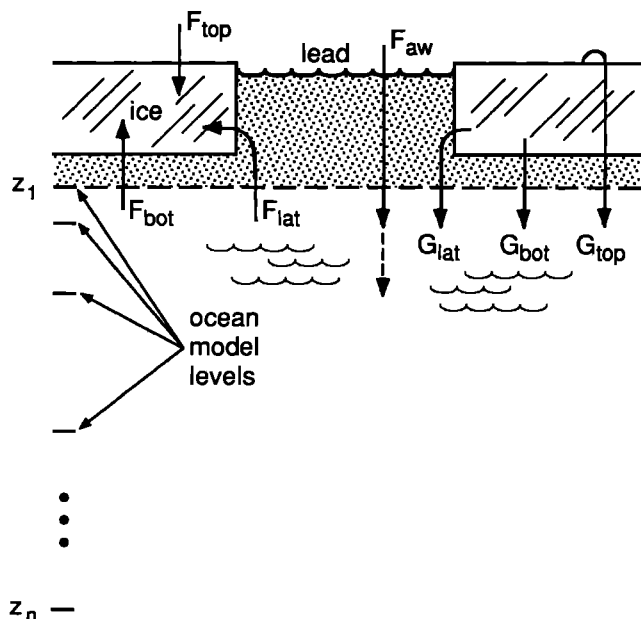

Fig. 4. Heat fluxes F and salt fluxes G in the ice-ocean model defined in the text. The heat (salt) flux is positive (negative) in the direction of the arrows. The air-water heat flux F_{aw} is a function of depth (denoted by dashed arrow) because of subsurface absorption of shortwave radiation. The numerical grid is also shown. The first level of the model lies below the ice bottom; i.e., we assume that the water above this point is uniformly well mixed.

Following MP87, the conductive heat flux through the ice is neglected in the "high summer" simulations discussed here. This means that the ice surface melt rate w_{top} is proportional to the net air-ice heat flux F_{top} via $w_{top} = -F_{top} / \rho_i Q$, where ρ_i is ice density (= 910 kg m^{-3}) and Q is the latent heat of fusion for sea ice. The latter quantity is a moderate function of the ice salinity [*McPhee and Untersteiner*, 1982], which varies with depth in thick ice. In the interest of simplicity, we use a fixed value of $Q = 2.92 \times 10^5$ J kg^{-1}, which corresponds to an ice salinity of 4 psu. The surface flux F_{top} is a combination of sensible, latent, and radiative contributions. We use the parameterizations of MP87 and the constants appropriate for their "cloudy, central Arctic" case, with the following exceptions. The incoming shortwave flux and surface air temperature are taken as the average values of the July and August observations by *Maykut*

[1982], or 181.75 W m^{-2} and $-1°C$, respectively; these values remain constant with respect to time over the integration. Also, a fixed wind speed of 6 m s^{-1} is used in the turbulent flux formulas. The ice albedo for ice thicker than 1.1 m is set to 0.64, which is the value for July used by *Maykut and Untersteiner* [1971] in their study of multiyear ice. The albedo decreases as the ice thins, in accord with the formula of *Perovich* [1983], down to a value of 0.48 at $H = 0.2$ m. Also, the ice temperature is set to $-1°C$. The decrease in ice thickness ΔH over a time step Δt due to surface melting is given by $\Delta H = \gamma \Delta t\, w_{top}$, where γ is the fraction of surface melt that is lost to runoff. (The rest remains on the surface as melt ponds and refreezes in the fall.) Following *Maykut and Untersteiner* [1971], we set $\gamma = 0.5$.

Similarly, the ice bottom melt rate w_{bot} is proportional to the ice-water heat flux at the ice bottom via $w_{bot} = -F_{bot} / \rho_i Q$. The flux F_{bot} is found by solving a system of ice-ocean boundary equations as described by *Mellor et al.* [1986], *McPhee et al.* [1987], and *Steele et al.* [1989b]. The solution assumes the existence of a molecular sublayer at the rough ice-ocean interface in which turbulent exchange is suppressed and molecular diffusion is dominant. The resulting melt rates for a given water temperature are reduced relative to the fully turbulent case. A simpler parameterization for bottom melting described by *McPhee* [1992] was also tested and yielded results similar to the full boundary layer solution.

The ice lateral melt rate w_{lat} is likewise proportional to the ice-water heat flux at floe edges via $w_{lat} = -F_{lat} / \rho_i Q$. However, this process is poorly understood in comparison with bottom melting. Several parameterizations for lateral melting are compared in Table 1. The table also shows the molecular sublayer formula used for bottom melting, which is based on laboratory experiments and has been tested both in the field [*McPhee et al.*, 1987] and in numerical models [*Riedlinger and Warn-Varnas*, 1990]. Table 1 shows that the simple *McPhee* [1992] formula produces results that are very similar to the full sublayer solution. The laboratory experiments of *Josberger and Martin* [1981] predict an order of magnitude less ablation than that given by the molecular sublayer formula. The *Perovich* [1983] model predicts lateral melt rates that are quite close to those of the molecular sublayer formula, and the MP87 formula predicts melt rates that are about 2.5 times stronger.

It is not immediately obvious how lateral melting relates to bottom melting. However, the fresh, buoyant meltwater behaves

TABLE 1. Lateral and Bottom Melt Parameterizations

Reference	Melt Rate	Formula	Sample Value, cm d^{-1}
Josberger and Martin [1981]	w_{lat}	$m_1 \Delta T^{m_3}$	0.28
Perovich [1983]	w_{lat}	$m_2 \Delta T^{m_3}$	1.55
Maykut and Perovich [1987]	w_{lat}	$m_1 u_\tau \Delta T^{m_4}$	4.61
Steele et al [1989a]	w_{bot}	$\dfrac{1}{A_T} u_\tau \Delta T/Q'$	1.78
McPhee [1992]	w_{bot}	$c_h u_\tau \Delta T/Q'$	1.59

Parameterizations depend on the elevation of the water temperature above the freezing point, ΔT, and the skin friction velocity u_τ, which in the final column are set to 0.2°C and 1 cm s^{-1}, respectively. The first formula for lateral melting and the first for bottom melting are from laboratory experiments; the others are from field data. The empirical constants $(m_1, m_2) = (0.3, 1.6) \times 10^{-6}$, $(m_3, m_4) = (1.36, 1.30)$, and $c_h = 0.0058$. The normalized latent heat is defined as $Q' \equiv rQ/c_w$, where $r = 0.9$ is the ratio of ice to water density and $c_w = 4218$ J kg^{-1}°C^{-1} is the heat capacity of water. The molecular sublayer factor $1/A_T$ is a function of the sublayer Reynolds and Prandtl numbers [*Steele et al.*, 1989a].

very differently in the two situations. During lateral melting, the more buoyant meltwater will rise along the vertical ice-water interface, allowing new, warm water to influence the ice. During bottom melting, the melt water is trapped at the horizontal ice-water interface; this trapping can be enhanced by the under-ice topography. Thus it seems reasonable to expect that lateral melt rates may be larger than bottom melt rates for the same thermal forcing. The additional effect of relative ice-ocean motion would tend to increase the flushing rate on both surfaces. In the simulations discussed in section 3, we compare results obtained by using (1) $w_{lat} = w_{bot}$, where w_{bot} is given by the molecular sublayer, and (2) w_{lat} as given by the formula of MP87.

Like MP87, we assume that lateral melting occurs uniformly over the entire lateral face of the ice floes (which we distribute over the thickness H, not just the draft $D \equiv \rho_i H / \rho_w$, where ρ_w is the water density). This will be true only for thermally well mixed leads, which, the observations of MP87 aside, may be more of a numerical convenience than a physical reality.

In summary, the sea ice equations of state comprise (7) and (8), which are prognostic equations for AH and A, along with the diagnostic equation (6c) for L. The thickness H is obtained by subtracting (8) from (7).

2.2. Ocean Model

The equations for ocean current u, temperature T, and salinity S are

$$\frac{\partial u}{\partial t} = ifu + \frac{\partial}{\partial z}\left[K_m \frac{\partial u}{\partial z}\right] \qquad (9a)$$

$$\frac{\partial T}{\partial t} = \frac{\partial}{\partial z}\left[K_h \frac{\partial T}{\partial z} + F_{sw}/\rho_w c_w\right] \qquad (9b)$$

$$\frac{\partial S}{\partial t} = \frac{\partial}{\partial z}\left[K_h \frac{\partial S}{\partial z}\right] \qquad (9c)$$

where $c_w = 4218$ J kg^{-1} °C^{-1} is the heat capacity of water. The current is given in complex notation as $u = (u_x, iu_y)$ and is computed only in order to obtain values for K_m and K_h. The latter are the viscosity and diffusivity coefficients, respectively, and are composed of turbulent and molecular contributions. The molecular effects become important only at the ice-ocean interface, as discussed by *Steele et al.* [1989a]. The turbulent coefficients are obtained via the level 2.5 turbulence-closure scheme of *Mellor and Yamada* [1982]. The procedure involves solving prognostic equations for the turbulent kinetic energy and turbulent length scale. This results in K_m and K_h that are functions of both depth and time (see *Steele et al.* [1989a] and *Mellor and Yamada* [1982] for details). An alternate method was also tested in which K_m and K_h were functions only of the surface stress [*Steele et al.*, 1989b], but this yielded unrealistically deep mixing in the presence of stabilizing melt fluxes. The Coriolis parameter is $f = 1.43 \times 10^{-4}$ s^{-1}, corresponding to a latitude of 80°.

The flux of shortwave energy that penetrates through the ice and into the leads is given by F_{sw}. The part penetrating the ice has been neglected in these simulations, since it is less than 1% of the flux predicted at the ice top surface when using the MP87 parameterization for 2- to 3-m-thick ice. The flux in the lead is a function of depth, with the surface value given by $F_{sw}(0) = (1 - \alpha_w)F_{sw}^0$, where $\alpha_w = 0.1$ is the water albedo and F_{sw}^0 is the incoming shortwave flux (= 181.75 W m^{-2}). The flux at levels below the surface is reduced by a logarithmic factor given by

MP87 for cloudy, central Arctic conditions. The flux at 3-m depth, for example, is about 38% of the surface value. Sensitivity studies showed that if the shortwave flux was assumed to occur only at the surface, melt rates were enhanced by about 10% and warming of the ocean column was reduced by about 35%.

2.3. Ocean Surface Boundary Conditions

The ocean surface stress is fixed at 0.1 N m^{-2} for all time, since we are not concerned here with the details of the momentum transfer between air, ice, and water.

The ocean surface heat flux F_{surf} is given by

$$F_{surf} = \left[(1-A)F_{aw}\right] + A\left[F_{bot} + \frac{\pi H}{\alpha L}F_{lat}\right] \qquad (10)$$

where F_{aw} is the net air-water heat flux in leads (including the shortwave flux $F_{sw}(0)$), as given by the parameterizations of MP87 with the modifications described previously. The shortwave flux dominates the air-water heat balance. The ice bottom and lateral fluxes F_{bot} and F_{lat} have been described previously. All of these fluxes are illustrated in Figure 4. The first term on the right-hand side of (10) represents the heat source for the ocean surface, and the terms in the second set of square brackets represent the heat sinks. Ocean heating results when the rate at which heat is input to the ocean surface is greater than the rate at which heat is lost as ice melts.

The ocean surface salt flux G_{surf} is given by

$$G_{surf} = A\left[G_{top} + G_{bot} + \frac{\pi H}{\alpha L}G_{lat}\right] \qquad (11)$$

where G_{top} is the salt flux associated with runoff from the ice top surface, and G_{bot} and G_{lat} are the salt fluxes associated with ice melting on the bottom and lateral surfaces, respectively. These fluxes are shown in Figure 4. Each of the terms on the right-hand side of (11) represents a freshwater flux to the ocean during the summer melt season.

The fluxes on the right-hand side of (11) are given by $G_j = 10^{-3}\rho_i \gamma_j \Delta S w_j$, where $j = $ (top, bot, lat), $\gamma_j = $ (0.5, 1, 1), and $\Delta S \equiv S_1 - S_j$. The salinities S_1 and S_j are defined as those at the uppermost grid point of the ocean model and in the sea ice, respectively. We set the latter to 4 psu. The density of sea ice ρ_i is 910 kg m^{-3}. The factor $\gamma_1 = 0.5$ accounts for runoff, as described previously. The units of salt flux are kilograms of salt per meter squared per second; fluxes are negative when ice melts.

2.4. Numerical Scheme

The numerical simulations assume horizontal homogeneity; thus the grid consists simply of 60 depth levels down to 100 m, which is deeper than the neutral Ekman layer depth for the given 0.1 N m^{-2} surface stress. Ocean properties (currents, temperature, and salinity) are staggered with respect to their fluxes (including the turbulence quantities such as the viscosity and diffusion coefficients K_m and K_h). The flux grid starts at a depth below the surface equal to the ice draft D plus the average sea ice roughness length z_0 (0.06 m) and increases in spacing exponentially from 0.01 m to 12 m (at the bottom). The property grid is defined at the midpoints of the flux grid. The integration is carried out for 60 simulation days, with a 30-min time step. Figure 4 illustrates the grid spacing in relation to the lead. We implicitly assume in this model that the water in the lead is homogeneous and is in fact well mixed with the water just under the ice bottom.

3. EXPERIMENTS AND RESULTS

The following numerical simulations are designed to simulate the decay of the sea ice cover during the height of the arctic summer. The simulations are run for 60 days corresponding to the months of July and August. The initial ice cover is specified as having an areal concentration of 90% and a thickness of 3 m. The initial floe diameter L_0 varies. The initial ocean state is quiescent, with a uniform salinity of 32 psu and a temperature at the freezing point. Motion is induced by linearly ramping up the ocean surface stress over the first inertial period, which reduces inertial ringing. The thermal forcing is similarly ramped up from inertial period 3 to period 4.

Each set of simulations described here consists of three cases, defined by an initial average floe diameter L_0 of 30 m, 300 m, and 3000 m. The geometrical factor $\pi H / \alpha L$ (equations (7) and (8)) for these cases is 0.476, 0.048, and 0.005, respectively. As a control, an additional simulation was performed in which lateral melting was not allowed, so that only ice thickness changed with time.

In the simulations, w_{lat} was given by either (1) the formula of MP87 (Table 1), or (2) w_{bot} using the molecular sublayer formula. Results are shown only for the former case. This is because changes in the thickness of the top and bottom surfaces were similar in both cases. Changes in floe diameter and concentration were not similar, however; the changes predicted for case 2 ($w_{lat} = w_{bot}$) can be obtained from (4) and (6c), respectively, given the change in thickness due to bottom melting.

Figure 5 shows the change in sea ice state parameters as a function of time. The change in ice concentration is a strong function of L_0. This is analogous to Figure 8 of MP87, in which the change in ice concentration is a strong function of the initial lead width. Thickness changes are partitioned about equally between bottom and top melting (which means that the top melting rate is actually twice as fast as the bottom when the factor γ is taken into account; see section 2.1). Average values of dL/dt in Figure 5 are 1.7 cm d^{-1}, which corresponds to $w_{lat} = 0.7$ cm d^{-1} using (4). That is, the rate at which a floe melts back laterally at any point along its perimeter is generally less than a centimeter per day. MP87 and *Hall and Rothrock* [1987] observed a variety of lateral melt rates in the warm (generally greater than 0°C) water of the MIZ, including short periods with rates as high as 40 cm d^{-1}. Melt rates were generally less than 10 cm d^{-1}, however.

When w_{lat} is set equal to w_{bot}, the changes in thickness are similar to those shown in Figure 5, with the same equal partition between top and bottom melting. On the other hand, the decrease in floe diameter at 60 days is less, about 0.5 m for all initial L_0; the decrease in concentration is (0.0286, 0.0029, 0.0003) for $L_0 =$ (30, 300, 3000) m. These values may also be derived simply from (4) and (6c), given that the floes melt about 0.2 m from the bottom in all cases.

The geometrical factor $\pi H / \alpha L$ gives the ratio between lateral and horizontal ice surface area. Sensitivity studies were run with $\alpha = 0.785$ (perfectly circular floes) and with $\alpha = 0.463$ (3 × 1 rectangular floes). The rate of concentration decrease is an inverse function of α via (8); however, the difference in ice concentration at 60 days between the two cases was only about 0.01 for $L_0 = 30$ m. Qualitatively, we expect that, in the absence of mechanical forcing, ice floes would become more circular as they melt and the rate of concentration decrease would slow down.

Figure 6 shows the oceanic response in terms of the temperature and salinity of the mixed layer. There is a layer of warmer, fresher water about 20 m deep embedded within the uniform initial ocean state which is produced by atmospheric heating and the
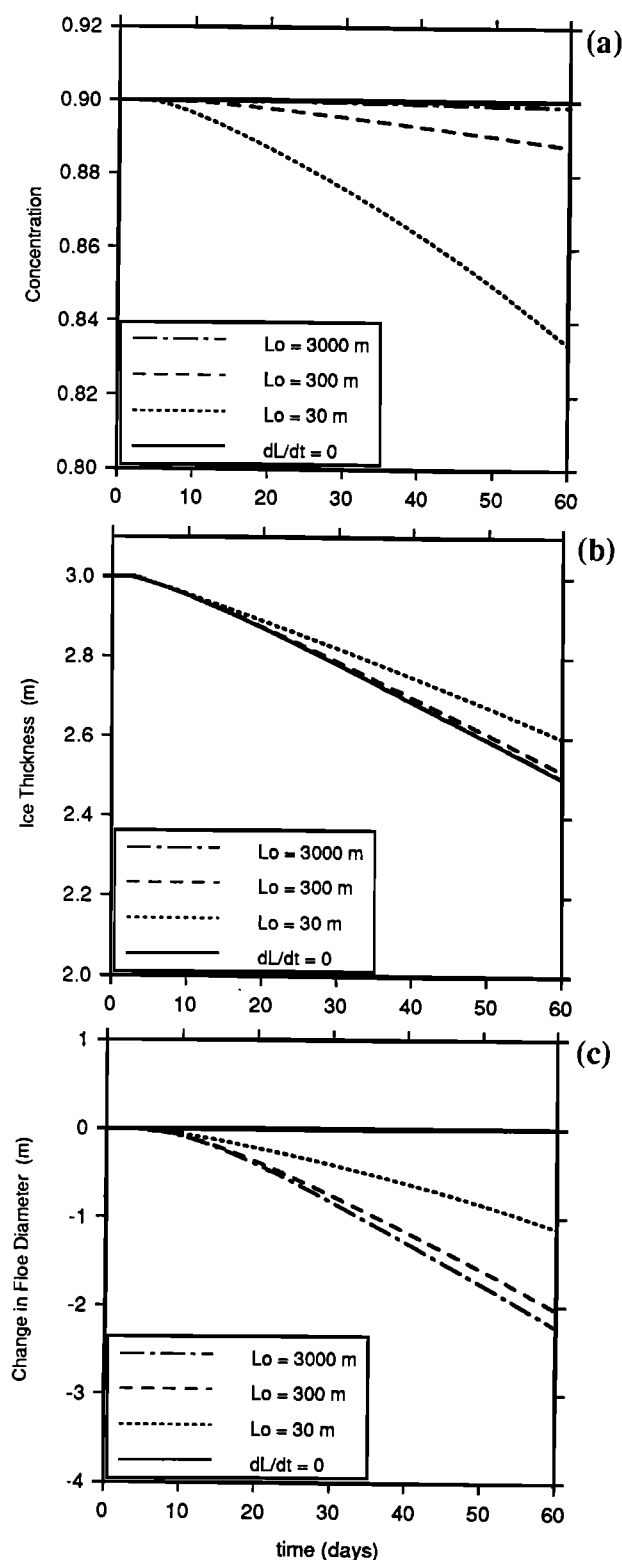

Fig. 5. Temporal changes in (a) ice concentration, (b) ice thickness, and (c) floe diameter. The ice concentration decreases most dramatically for small floes.

resulting ice melting. Its depth is defined here as the level at which the turbulent kinetic energy is reduced to 10% of its surface value [*Martin*, 1985]. Note from Figure 6 that the mixed layer is coldest and freshest when $L_0 = 30$ m. More melting occurs here than in the other cases because of the larger amount of ice-ocean interface.
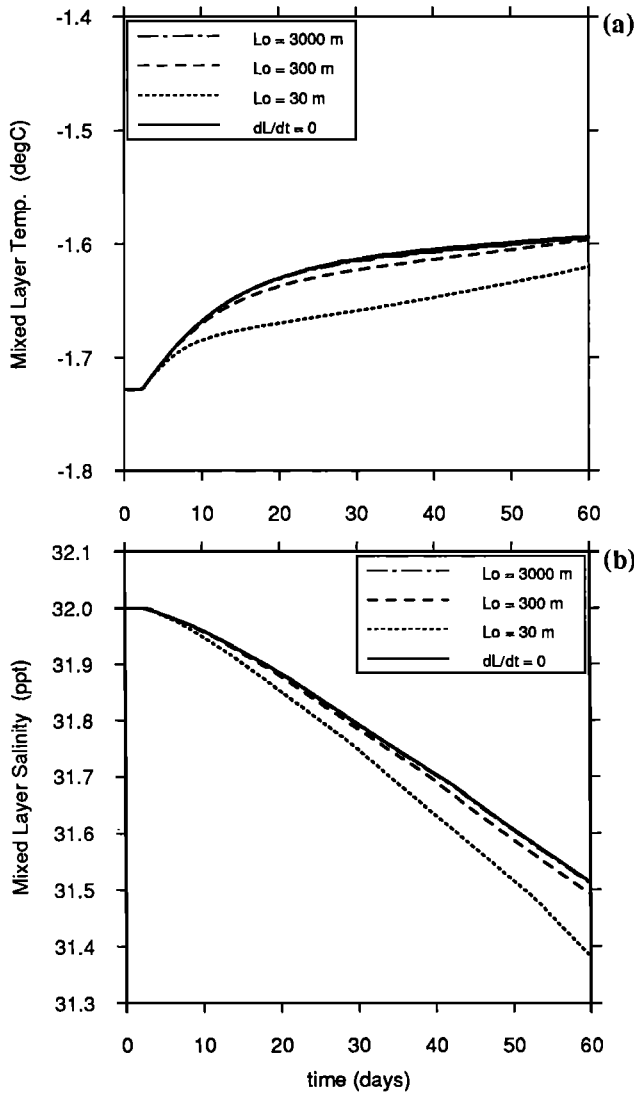
Fig. 6. Temporal changes in (a) temperature and (b) salinity of the oceanic mixed layer. Atmospheric heating and resulting ice melting lead to a relatively warm, fresh mixed layer.

Let us now consider the heat and salt budgets in the ocean. Using (10) and integrating (9b) over the depth of our domain, we obtain

$$(1 - A)f(0) = \dot{E} - A(w_{bot} + \frac{\pi H}{\alpha L}w_{lat}) \qquad (12)$$

where, following the notation of MK89 and H79, $f(0) \equiv F_{aw}(0)/\rho_i Q$, where $F_{aw}(0)$ is the air-water heat flux at the ocean surface. The temporal change in the heat content of the water column, divided by the factor $\rho_i Q$, is given by $\dot{E}$. Note that the heat flux at the bottom of the numerical domain (100 m depth) is set to zero. We see from (12) that the total heating contributes to three processes: ocean warming, bottom melting, and lateral melting. Figures 7b and 8b compare these processes for initial floe diameters of 30 m and 300 m, normalized by the total heating. Figures 7a and 8a show the total heating, given by the left-hand side of (12), which increases with time as A decreases owing to lateral melting. Figures 7c and 8c show the freshwater fluxes due to melting from top, bottom, and lateral ice surfaces, normalized by the total at each time step.

Lateral melting plays a major role only for the smaller floes. Approximately 20% of the net forcing goes into warming the ocean. (This is reduced to about 10% when the shortwave flux is assumed to occur only at the ocean surface.) This result is in contrast to many ocean models which assume that the ocean remains at the freezing point as long as ice exists in the domain (i.e., $\dot{E} \equiv 0$ for all time). Also note that, for larger floes, the freshwater fluxes (Figures 7c and 8c) are about equally distributed between top and bottom melting.

To examine these issues further, we divide (12) by the left-hand side $(1 - A)f(0)$ to obtain two nondimensional quantities,

$$\Phi_{bot} \equiv \frac{Aw_{bot}}{(1 - A)f(0)} = \frac{A\dot{H}_{bot}}{(1 - A)f(0)} \qquad (13a)$$

and

$$\Phi_{lat} \equiv \frac{A_L w_{lat}}{(1 - A)f(0)} = \frac{H\dot{A}}{(1 - A)f(0)} \qquad (13b)$$

where Φ_{bot} and Φ_{lat} are the fraction of incoming heat at the ocean surface that is used in bottom and lateral melting, respectively. The lateral surface concentration A_L was defined just after (6). The second equalities in (13a) and (13b) use (7) and (8), where the dot indicates time rate of change. The results are plotted in Figure 9 for the same L_0 shown in Figures 7 and 8. Note that Φ_{lat} is equivalent to the parameter Φ_m of MK89. In lieu of an explicit parameterization for ice floe geometry such as presented here, the MK89 and H79 models assign a fixed value of $\Phi_{bot} = \Phi_{lat} = 0.5$ (considering only the part of their versions of (7) and (8) that depends on atmospheric heat flux $f(0)$). For comparison, the value $\Phi = 0.5$ is plotted in Figure 9. The partition is about 50:50 only for the smallest floes. For larger floes, much more heat is lost via bottom melting than via lateral melting because of the relative amounts of horizontal and lateral surface areas.

Because MP87 included no explicit ocean model, they necessarily defined a constant R that described the percentage of heat in the water column that returns to the ice bottom per unit time. In terms of (12), $R \equiv -Aw_{bot}/\dot{E}$. The R values calculated for the present simulation are shown in Figure 10 in units of percent per day for w_{lat} given by the MP87 parameterization. The results are similar when w_{lat} is given by the molecular sublayer formula. MP87 used $R = 50\%$ d^{-1}. The model discussed here indicates that MP87 overestimated the rate at which oceanic heat is transferred to the ice bottom; McPhee et al. [1987] also found this to be the case when the molecular sublayer was neglected. In fact, a simple estimate for R is easily obtained using the McPhee [1992] parameterization (Table 1) for F_{bot} ($= \rho_i Q w_{bot}$),

$$R = \frac{Ac_h u_\tau}{MLD_T} \qquad (14)$$

where the heat in the water column $E/\rho_i Q$ has been parameterized for the sake of this argument as nonzero only within a thermal mixed layer MLD_T. (This is deeper than the usual mixed layer owing to subsurface absorption of shortwave energy.) For $A = 0.9$, $c_h = 0.0058$, $u_\tau = 0.01$ m s^{-1}, and $MLD_T = 40$ m, $R = 11\%$ d^{-1}.

4. DISCUSSION

We return now to our original question: "How important is lateral melting in the total volume melted from sea ice floes?" Figure 11 shows the melting from top, bottom, and lateral surfaces over the 60-day integrations. Lateral melting is important

Ocean heating

a

Heat flux (W·m⁻²)

time (Days)

Thermal response (normalized)

b

Ocean warming

Lateral melt

Bottom melt

Heat flux

time (Days)

Freshwater fluxes (normalized)

c

Runoff

Lateral melt
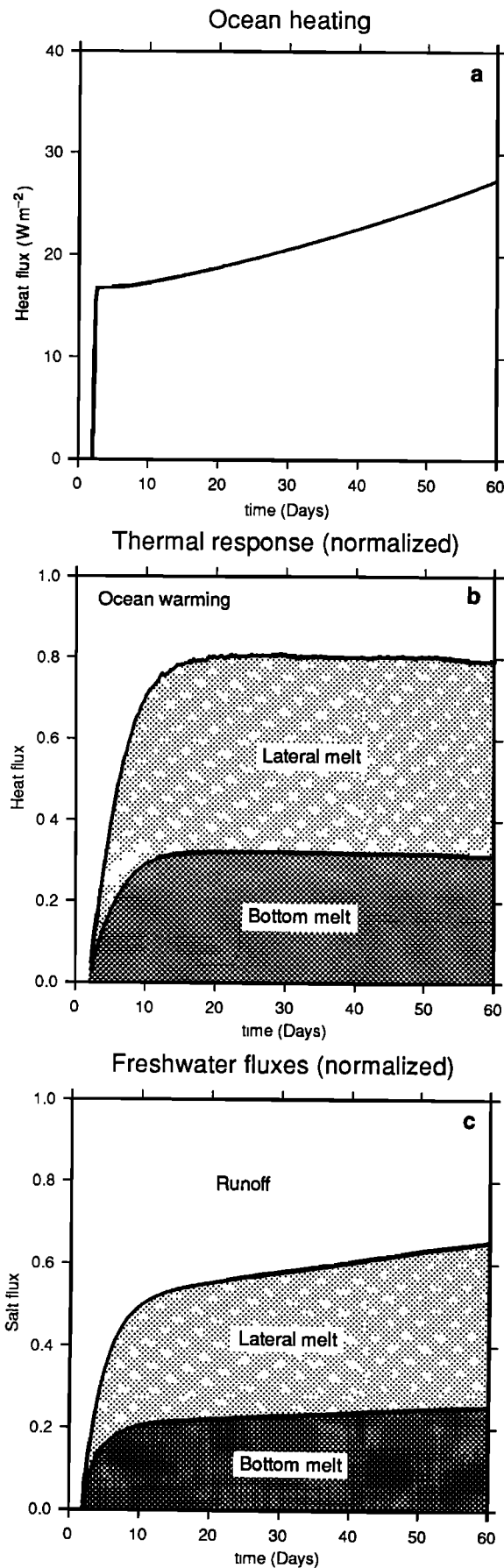
Bottom melt

Salt flux

time (Days)

Fig. 7. Ocean heat and salt budgets for initial floe diameter $L_0 = 30$ m. (a) Total heating, which increases with time as ice concentration decreases. (b) Thermal response normalized by the total input from Figure 7a and stacked vertically to sum to 1.0. Ocean warming takes about 20% of the incoming energy, and lateral melting about 50%. (c) Freshwater fluxes due to top, bottom, and lateral melting normalized by the total at each time.

Ocean heating

a

Heat flux (W·m⁻²)

time (Days)

Thermal response (normalized)

b

Ocean warming

Lateral melt

Bottom melt

Heat flux

time (Days)

Freshwater fluxes (normalized)

c

Runoff
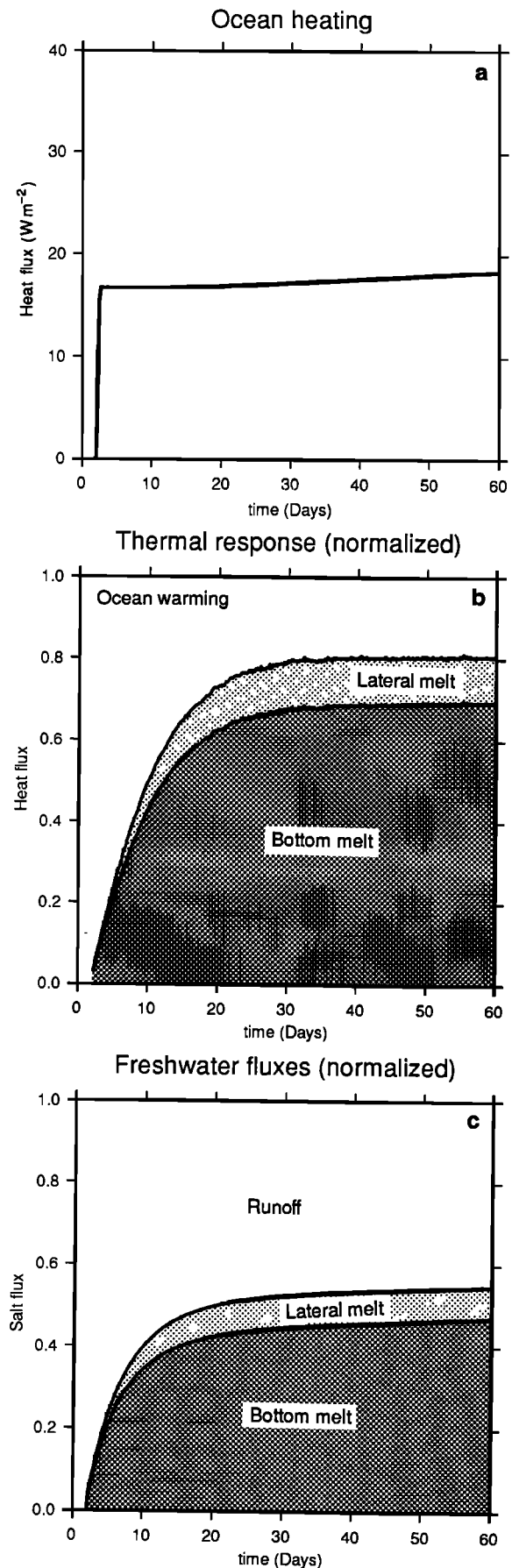
Lateral melt

Bottom melt

Salt flux

time (Days)

Fig. 8. Same as Figure 7, but for initial floe diameter $L_0 = 300$ m. Lateral melting is much less significant than in Figure 7.
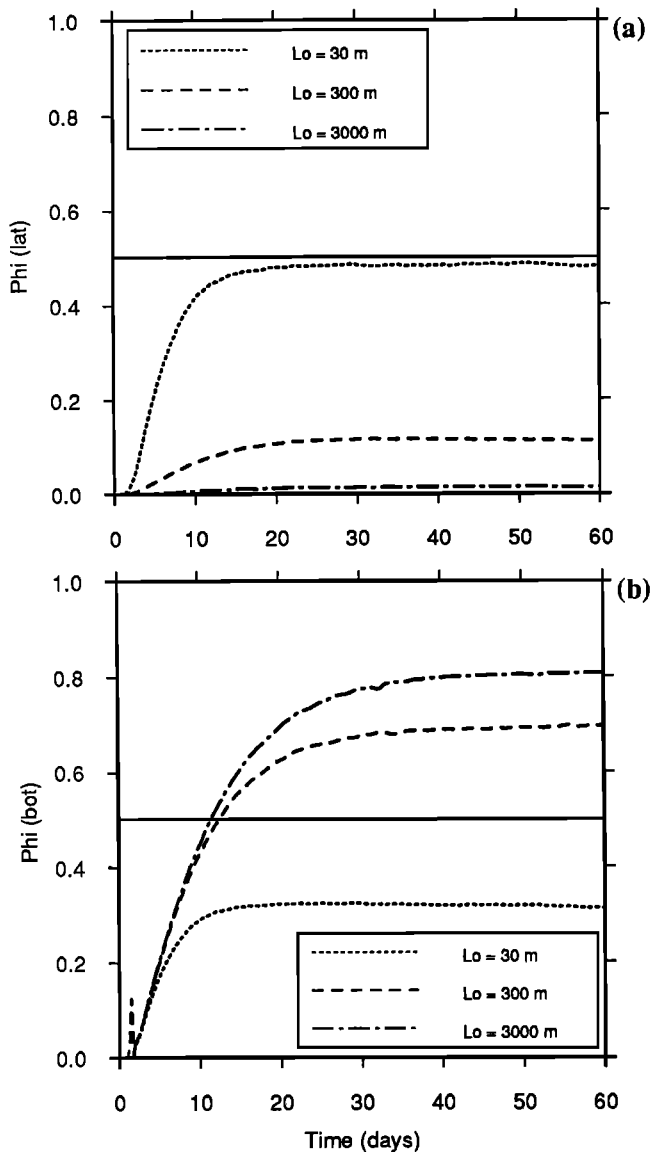
Fig. 9. The fraction of incoming heat at the ocean surface that goes (a) to lateral melting (Φ_{lat}) and (b) to bottom melting (Φ_{bot}). For comparison, the value used by many ice-ocean models is plotted at 0.5. The partition between lateral and bottom melting is a strong function of floe diameter.

Fig. 10. The percent of thermal energy in the ocean that is lost to ice bottom melting per day, R. The molecular sublayer slows down this process relative to a fully turbulent simulation.

Fig. 11. The percent of melting from each ice floe surface (top, bottom, and lateral) that occurs over the course of the 60-day simulation as a function of initial diameter. Surface melting is strongest, followed by bottom and then lateral melting for all but the smallest floes. The total melting during each simulation can be expressed in terms of the change in ice volume per unit area $\Delta(H/A)$ over the 60-day integration. For initial floe diameters L_0 of 30 m, 300 m, and 3000 m, these are 0.54 m, 0.47 m, and 0.42 m, respectively. More total melting occurs when floes are small.

only for L_0 = 30 m. (It was even less when the molecular sublayer parameterization was used for w_{lat}, not shown.) Top surface melting is roughly equal to bottom surface melting for the larger floes, although this is sensitive to the runoff factor γ. (When $\gamma = 0$ following MP87, top melting is about twice bottom melting, in accord with the results shown in their Table 3.) The total amount of ice melted in each case is an inverse function of the initial floe diameter.

Figure 5 showed that the change in ice concentration A over the 60-day simulation was a strong function of L_0, the initial average floe diameter. A field of uniformly small floes, such as can be observed in the MIZ, will melt faster (with respect to a decrease in A) than one of large floes. This also applies to a uniform distribution of floe sizes (Figure 3b), where L_0 is taken to mean the initial average diameter. Note that the atmospheric thermal forcing used here was typical of conditions in the central Arctic; in the MIZ, the atmospheric forcing will be stronger and will be enhanced by the presence of warm ocean currents.
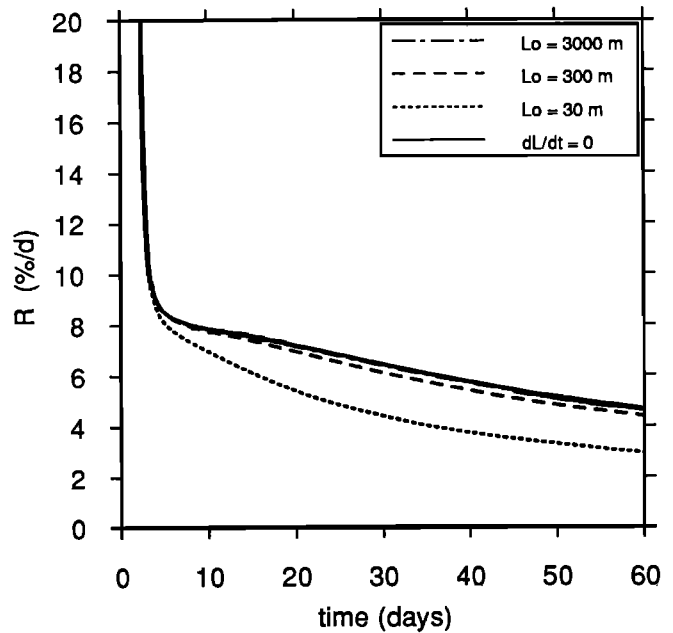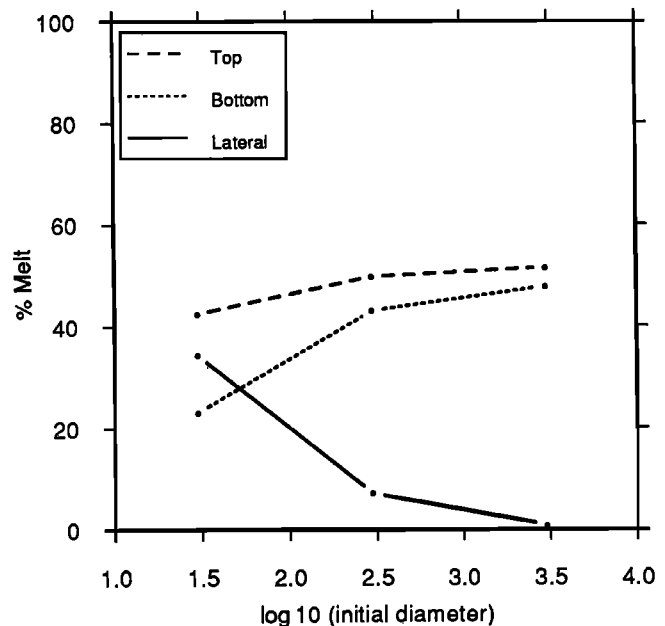
In the distribution calculated from Figure 1 for a region in the Beaufort Sea (Figure 3c), there were many more small floes than large floes; however, the concentration of floes with diameters from 30 m to 300 m is only about 5%. Thus the change in total concentration A due to lateral melting would be small, even if these floes melted completely away. A more realistic estimate can be obtained by differentiating (6c) with respect to time and using $\Delta L = 2$ m and an average diameter of 30 m; this yields a

concentration change of about 0.007, i.e., less than 1%. Note that floes with diameters smaller than 30 m were not digitized from Figure 1 and thus are not included in these results. They constitute at most 12% of the area, given that the ice concentration for floes with diameters greater than 30 m is about 88%.

Figure 1 is, of course, just one realization of the floes in a certain part of the Arctic on a particular day. It is likely that the distribution as well as the geometrical factors used in (1) and (2) may change during the course of the summer. Regional differences may also be important. Finally, the role of mechanical breaking (by floe-floe interaction) has been neglected in these simulations. The process has been modeled by *Lensu* [1989]. As was noted by *Thorndike et al.* [1975, p. 4501], "The thermodynamics seeks the mean and the mechanics [seeks] the extremes." In the present context, this means that melting acts as a sink for smaller floes, while mechanical breaking offsets this effect to some degree by redistributing the larger floes into smaller floes. Thus the scene in Figure 1 could be maintained by a strong source of very small floes with diameters of only a few meters or less (mechanical breaking) working simultaneously with a large sink (melting). These processes might be separated by studying successive images taken during and after a storm. The mechanical forcing would presumably create many small floes which would then melt over the next several days.

It is often assumed by numerical modelers that no heat contributes to warming the ocean until all the ice in a grid cell disappears [e.g., *Lemke et al.*, 1990]; this is at odds with the observations of MP87 and with the results of the present simulations. Leads, in fact, rise above the freezing point in the summer, and this affects both melt rates and the air-water energy balance. The present model predicts that about 20% of the atmospheric heat flux is stored in the water column during ice melting.

Finally, note that the present model may underestimate the amount of heat that goes into decreasing the concentration *A*, by assuming that the water in leads and under the floes is well mixed. If the wind stress is low and the floes are large, the water in leads will be stratified [*Perovich*, 1983], and heat may be preferentially deposited on floe edges. Also, surface waves in leads can accelerate lateral melting near the floe surface. If the water in the lead is thermally stratified, lateral melting will be nonuniform, resulting in an ice face that departs significantly from the vertical (MP87). This effect is no doubt enhanced by the subfreezing temperatures observed near the surface of thick ice in early summer, which delays ice melting there.

REFERENCES

Bourke, R. H., and R. P. Garrett, Sea ice thickness distribution in the Arctic Ocean, *Cold Reg. Sci. Technol.*, *13*, 259–280, 1987.

Hall, R. T., and D. A. Rothrock, Photogrammetric observations of the lateral melt of sea ice floes, *J. Geophys. Res.*, *92*, 7045–7048, 1987.

Hibler, W. D., A dynamic thermodynamic sea ice model, *J. Phys. Oceanogr.*, *9*, 815–846, 1979.

Josberger, E. G., and S. Martin, A laboratory and theoretical study of the boundary layer adjacent to a vertical melting ice wall in salt water, *J. Fluid Mech.*, *111*, 439–473, 1981.

Lemke, P., W. B. Owens, and W. D. Hibler, A coupled sea ice–mixed layer–pycnocline model for the Weddell Sea, *J. Geophys Res*, *95*, 9513–9525, 1990.

Lensu, M., The random breakage of ice, in Regional and Mesoscale Modelling of Ice Covered Oceans, NRSC Conf. Rep. 3, Nansen Remote Sens. Cent., Bergen, Norway, 1989.

Martin, P., Simulation of the mixed layer at OWS November and Papa with several models, *J. Geophys. Res.*, *90*, 903–916, 1985.

Maykut, G. A., Large-scale heat exchange and ice production in the central Arctic, *J. Geophys. Res.*, *87*, 7971–7984, 1982.

Maykut, G. A., and D. K. Perovich, The role of shortwave radiation in the summer decay of a sea ice cover, *J. Geophys. Res*, *92*, 7032–7044, 1987.

Maykut, G. A., and N. Untersteiner, Some results from a time-dependent thermodynamic model of sea ice, *J. Geophys. Res*, *76*, 1550–1575, 1971.

McPhee, M. G., Turbulent heat flux in the upper ocean under sea ice, *J. Geophys. Res.*, *97*, 5365–5379, 1992.

McPhee, M. G., and N. Untersteiner, Using sea ice to measure vertical heat flux in the ocean, *J. Geophys. Res.*, *87*, 2071–2074, 1982.

McPhee, M. G., G. A. Maykut, and J. H. Morison, Dynamics and thermodynamics of the ice/upper ocean system in the marginal ice zone of the Greenland Sea, *J. Geophys. Res.*, *92*, 7017–7031, 1987.

Mellor, G. L., and L. Kantha, An ice-ocean coupled model, *J. Geophys. Res.*, *94*, 10,937–10,954, 1989.

Mellor, G. L., and T. Yamada, Development of a turbulence closure for geophysical fluid problems, *Rev. Geophys.*, *20*, 851–875, 1982.

Mellor, G. L., M. G. McPhee, and M. Steele, Ice-seawater turbulent boundary layer interaction with melting or freezing, *J. Phys. Oceanogr*, *16*, 1829–1946, 1986.

Perovich, D. K., On the summer decay of a sea ice cover, Ph.D. dissertation, Univ. of Wash., Seattle, 1983.

Riedlinger, S. H., and A. Warn-Varnas, Predictions and studies with a one-dimensional ice-ocean model, *J. Phys. Oceanogr.*, *20*, 1545–1562, 1990.

Rothrock, D. A., and A. S. Thorndike, Measuring the sea ice floe size distribution, *J. Geophys. Res.*, *89*, 6477–6486, 1984.

Steele, M., G. L. Mellor, and M. G. McPhee, The role of the molecular sub-layer in the melting or freezing of sea ice, *J. Phys. Oceanogr.*, *19*, 139–147, 1989a.

Steele, M., J. H. Morison, and N. Untersteiner, The partition of air-ice-ocean momentum exchange as a function of ice concentration, floe size, and draft, *J. Geophys. Res.*, *94*, 12,739–12,750, 1989b.

Thorndike, A. S., D. A. Rothrock, G. A. Maykut, and R. Colony, The thickness distribution of sea ice, *J. Geophys. Res.*, *80*, 4501–4513, 1975.

Wadhams, P., V. A. Squire, D. J. Goodman, A. M. Cowan, and S. C. Moore, The attenuation rates of ocean waves in the marginal ice zone, *J Geophys. Res.*, *93*, 6799–6818, 1988.

M. Steele, Polar Science Center, Applied Physics Laboratory, HN-10, University of Washington, 1013 NE 40th Street, Seattle, WA 98105-6698.